Calibration of a Telecentric Structured-Light Device for Micrometric 3D Reconstruction

Mara Pistellato[1][a], Andrea Albarelli[1][b] and Filippo Bergamasco[1][c]
[1]*DAIS, Università Ca'Foscari Venezia, 155, via Torino, Venezia Italy*
{*mara.pistellato, filippo.bergamasco, albarelli*}*@unive.it*

Keywords: Camera-projector Calibration, Structured-light Scanning, Telecentric Lenses, Micrometric Surface Reconstruction.

Abstract: Structured-light 3D reconstruction techniques are employed in a wide range of applications for industrial inspection. In particular, some tasks require micrometric precision for the identification of microscopic surface irregularities. We propose a novel calibration technique for structured-light systems adopting telecentric lenses for both camera and projector. The device exploits a fixed light pattern (striped-based) to perform accurate microscopic surface reconstruction and measurements. Our method employs a sphere with a known radius as calibration target and takes advantage of the orthographic projection model of the telecentric lenses to recover the bundle of planes originated by the projector. Once the sheaf of parallel planes is properly described in the camera reference frame, the triangulation of the surface's object hit by the light stripes is immediate. Moreover, we tested our technique in a real-world scenario for industrial surface inspection by implementing a complete pipeline to recover the intersections between the projected planes and the surface. Experimental analysis shows the robustness of the proposed approach against synthetic and real-world test data.

1 INTRODUCTION

Structured-light approaches adopt a controlled light source with known geometry to locate the same material point from different views, recovering its depth via triangulation (Pistellato et al., 2015). A classical example is the well-known phase-shift method (Zuo et al., 2018; Pistellato et al., 2018), widely used in several applications with appropriate unwrapping algorithms (Pistellato et al., 2019a; Pistellato et al., 2019b). Such approaches are portable solutions which can be easily integrated in industrial settings, allowing for high precision measurements without touching the artefact (Xu et al., 2011b; Xu et al., 2011a). In these scenarios the adoption of a precise measurement system is a key element to assess the quality of the manufactured objects during construction, specially because an accurate and extensive control also reduces potential issues that may emerge during the subsequent production steps.

Fringe projection is often employed in the context of microscopic applications, where the acquired

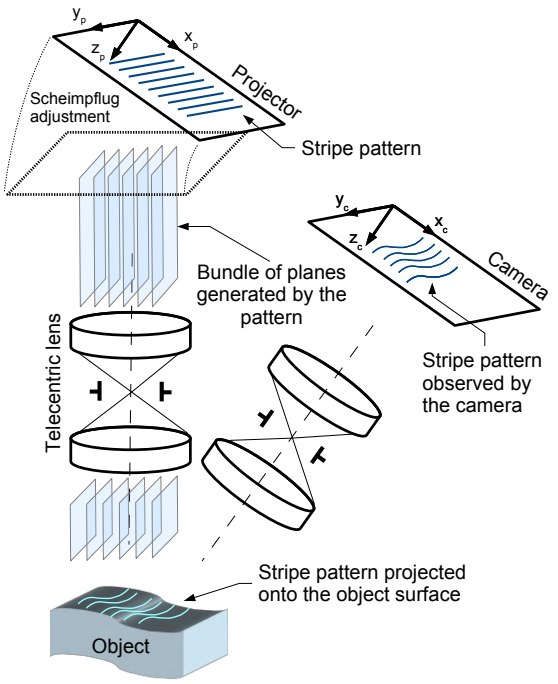

Figure 1: Picture and geometric schema of our telecentric camera-projector 3D reconstruction device.

[a] https://orcid.org/0000-0001-6273-290X
[b] https://orcid.org/0000-0002-3659-5099
[c] https://orcid.org/0000-0001-6668-1556

object features' size ranges from millimetres to microns. This is the case of several tasks, as quality control (Weckenmann et al., 2006), weld pool surface depth measurement (Saeed and Zhang, 2007), laminated plastic wrinkles evaluation (Yao and Xu, 2007), electrical components or small coins reconstruction (Li et al., 2014; Liu et al., 2015). Additional examples include the work presented in (Bergström et al., 2011; Rosendahl et al., 2010) for an object shape verification system using structured-light and stereo correspondences, while (Li and Zhang, 2017), proposes to combine fringe projection with binary defocusing technique (Lei and Zhang, 2009) for 3D microscopic profilometry. When the acquisition speed is a limiting factor, fixed patterns are typically used in the form of random distributions (Chen et al., 2018) or binary and coloured codes (Zhou et al., 2017). Shape from single stripe pattern is proposed in (Winkelbach and Wahl, 2002), where authors devise surface normals from the stripes observed by a single camera. All the aforementioned applications require an initial calibration to assess the geometric relations between the components involved in the acquisition.

Such process has a direct impact on the quality of the reconstruction, particularly for industrial-related applications, where accuracy is a critical requirement. In the specific case of telecentric surface reconstruction, the narrow field-of-view of the lenses requires a specialised method as well as a specifically-designed calibration target. Common approaches can employ a small planar target with a grid dot pattern that can be easily detected and identified by the imaging system (Li et al., 2014; Li and Zhang, 2015; Chen et al., 2014; Bergamasco et al., 2011), complex 3D targets (Liu et al., 2017), or none (Bergamasco et al., 2014).

In this paper we describe a structured-light device based on telecentric fringe projection profilometry for micrometic measurements. Our setup combines a telecentric camera and projector with a fixed pattern composed by equally spaced parallel lines. Both camera and projector imaging systems are affected by negligible lens distortion and are characterised by an orthographic projection model. The advantages of employing a single striped pattern are several: first, we need a single shot to reconstruct the scene, thus the acquisition and computation speed are significantly increased. Moreover, the system does not require accurate gamma calibration and it does not suffer from particular scene features like non-uniform albedo or materials. The contribution is twofold: first, we propose a novel calibration solution involving the observation of a sphere with a known radius in different positions. The intersections of the parallel planes generated by the projected pattern with the spherical surface originate a series of coaxial 3D circles that are projected as ellipses on the camera image plane. Such curves can be exploited to geometrically compute the system parameters and obtain the correct pixel scale by fitting the 3D sphere. The second contribution consists in a specific case-of-study where the described sensor is employed to reconstruct the internal surface of industrial gearwheels. The overall accuracy and low cost of such approach makes it a potential substitute for the classic contact measuring for quality assessment in industrial applications. Indeed, it is particularly suitable for the inspection of smooth surfaces requiring micrometric precision.

2 CALIBRATION TECHNIQUE

Considering their orthographic imaging model, telecentric lenses are particularly convenient to measure small objects. In an orthographic camera the centre of projection is located at infinity, so that rays coming from the captured object intersect the image plane orthogonally (Hartley and Zisserman, 2003). This implies that the projection on the image plane is not affected by the object's depth, and thus the size of each pixel corresponds to a certain length in the real world, making straightforward to measure distances along x and y axes. On the other hand, depth computation and 3D reconstruction are not immediate and require specialised approaches.

Our device is sketched in Figure 1: the projector casts on the scene a fixed pattern consisting in a series of equally-spaced straight lines. Such lines generate a bundle of equispaced parallel planes $\mathcal{P}$ in 3D space, that are orthogonal to the projector's image plane. We define the *stride* Δ as the distance between any two consecutive planes. This value is proportional to the lines distance on the projector's image plane, but it is scaled by a multiplicative unknown factor. Such scale depends on the combination of (i) the magnifying factor of the telecentric lens and (ii) the inclination of the projector's focus plane (Scheimpflug adjustment), that needs to be aligned with the camera image plane to obtain the optimal depth-of-field.

The planes orientation with respect to the camera coordinate system and their stride are unknown, thus we identify three parameters that need to be estimated by the calibration process:

1. the normal vector $\mathbf{n} = \begin{pmatrix} n_x & n_y & n_z \end{pmatrix}^T$ of all the parallel planes in the bundle $\mathcal{P}$ with respect to the camera reference frame;
2. The scale factor s between camera pixels and the real world units (i.e. pixel's size in millimetres).
3. The *stride* Δ.

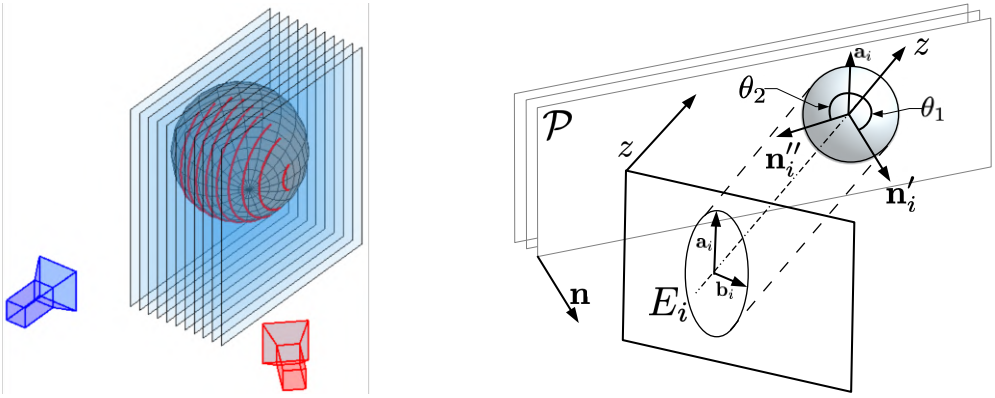

Figure 2: Left: telecentric projector (in blue) generates a parallel sheaf of planes $\mathcal{P}$ intersecting a known sphere used as calibration target. Such intersections result in coaxial circles in space which (due to self-occlusions) are observed as a set of arcs by the camera. Right: each circle is projected to the image plane as the ellipse E_i. The normal $\mathbf{n}$ can be obtained by rotating the vector z around the axis $\mathbf{a}_i$, but two alternative solutions ($\mathbf{n}'$ and $\mathbf{n}''$) are equally valid and must be disambiguated.

All the planes in the bundle are identical, and therefore is not possible to distinguish their absolute offset (or numbering) within the projector image plane. For this reason, we assume to only recognise their relative order (i.e. which one comes after another) but not their absolute index with respect to the first one, which generally depends by the depth of the observed object. So, without loss of generality, we can assume that $\mathcal{P}$ contains an infinite set of planes $P_1 = (p_1, \mathbf{n}), P_2 = (p_2, \mathbf{n}), \ldots$ (parameterised as a point p_i and the normal vector $\mathbf{n}$) such that $p_i = \Delta \mathbf{n} i$.

During the calibration process, a sphere with known radius r is imaged so that a subset of N planes originated from the projector are cast on the sphere's surface. The intersection of parallel planes with with the sphere generates N circles in 3D space that exhibit some particular properties: (i) they are are coaxial since all the slicing planes are parallel, (ii) their 3D centres lie on a line L in space, and (iii) L is orthogonal to the parallel sheaf of planes (i.e. line direction has the same orientation as $\mathbf{n}$). Since the sphere self-occludes the projected light rays, only N arcs $\mathcal{A}_1 \ldots \mathcal{A}_N$ of the full circles are visible on the surface. Such N 3D circle arcs are therefore imaged by the camera as portions of N 2D ellipses $E_1, ..., E_N$. For each ellipse E_i with $i = 1, ..., N$, the plane bundle normal vector $\mathbf{n}$ can be recovered up to two equally possible configurations.

Let $\mathcal{C}_i$ be the i^{th} circle generated by the intersection of the i^{th} plane in $\mathcal{P}$ and the sphere. Since we are using an orthographic camera, $\mathcal{C}_i$ projects to an ellipse E_i having $\mathbf{a}_i$ and $\mathbf{b}_i$ as major and minor axes respectively (see Fig. 2). The length of $\mathbf{a}_i$ is equal to the radius r of the sphere, so if we rotate the bundle of planes $\mathcal{P}$ around the axis $\mathbf{a}_i$ the eccentricity of E_i changes. In particular, as shown in (Bergamasco et al., 2020; Pistellato et al., 2019c), the ratio between the semi-axes is a function of the angle θ between the normal $\mathbf{n}$ and the camera z-axis:

$$cos\,\theta = \frac{||\mathbf{b}_i||}{||\mathbf{a}_i||}. \tag{1}$$

In this setting, the bundle normal $\mathbf{n}$ can be obtained by rotating the vector $z = (0,0,1)^T$ around the axis $\mathbf{a}_i$ with two equally possible angles:

$$\theta_{1,2} = \pm arccos \frac{||\mathbf{b}_i||}{||\mathbf{a}_i||}. \tag{2}$$

As a consequence, each ellipse E_i generates two equally possible normal vectors $\mathbf{n}'_i$ and $\mathbf{n}''_i$. Note that also $-\mathbf{n}'_i$ and $-\mathbf{n}''_i$ are valid solutions but can be ignored in the disambiguation process since they represent the same plane.

The 3D line L connecting all the circles' centres projects onto the camera image plane as the 2D line l passing through the ellipses centres. The disambiguation of the correct $\mathbf{n}$ exploits the geometry of l to filter out the wrong plane normals. Indeed, we recall that $\mathbf{n}$ is parallel to the axis L and that all normal vectors generated by the N ellipses must be oriented to the same direction. So, among all the alternatives, we keep the normal vectors whose angles formed with the axis L is minimum.

Finally, since the ellipses centres are the orthographic projections of the 3D circles centres, the stride value can be computed from the relative distance (in pixels) between adjacent ellipses centres on the image plane. The relation between such distance and the stride value is the following:

$$\Delta = \frac{d}{sin(\beta)} \tag{3}$$

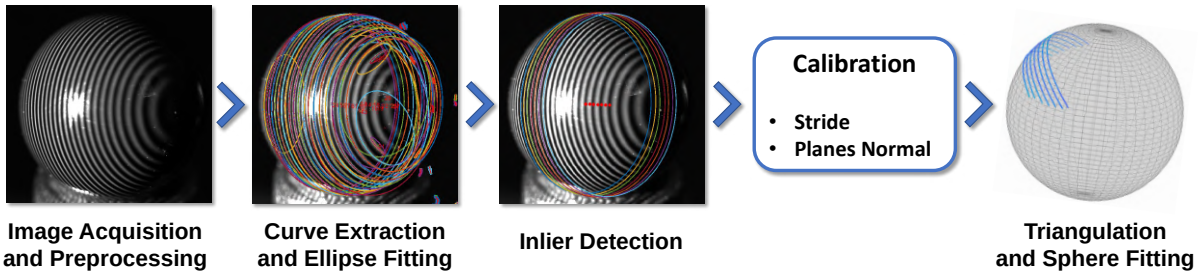

Figure 3: Our proposed calibration pipeline. From left to right: (i) Stripe pattern is projected and a known calibration sphere is exposed to the camera in different positions. Thresholding, skeletonization, and filtering is applied to cluster each arc. (ii) Ellipses are robustly fitted to arc points (via RANSAC) and a selection procedure is used to extract a subset of inlier ellipses whose centers are uniformly distributed on a straight line. (iii) Plane bundle stride and normal is estimated is §2. (iv) 2D arc points are triangulated by intersecting the corresponding exiting camera rays with the recovered plane bundle. A sphere is fitted to the obtained 3D points.

where β is the angle formed by the plane normal $\mathbf{n}$ and the camera z-axis, and d is the distance (in camera pixels) between two consecutive projected centres. Note that, due to the orthographic projection, this is the equivalent of computing the hypotenuse of a right-angled triangle.

Once the stride Δ and plane normal $\mathbf{n}$ are computed, points composing the 3D arcs $\mathcal{A}_1 \dots A_N$ can be triangulated by simply intersecting the exiting camera rays passing through ellipses $E_1 \dots E_N$ with the 3D planes in $\mathcal{P}$. Let $e_i^j \in \mathbb{R}^2$ be the j^{th} 2D point of the ellipse E_i. Its $3D$ position g_i^j is given by:

$$g_i^j = \frac{(p_i - e_i^j)^T \mathbf{n}}{n_z} \begin{pmatrix} 0 \\ 0 \\ 1 \end{pmatrix} e_i^j. \tag{4}$$

The obtained point cloud is then fitted to a sphere model S, obtaining a radius r_S, expressed in camera pixels. Since the acquired sphere has known radius, the scale between pixels and world units is simply given by

$$s = \frac{r}{r_S}. \tag{5}$$

Finally, to obtain a robust parameter estimation the procedure is repeated for different sphere locations. The final parameters are computed by averaging the resulting values, excluding the acquisitions for which the RMS of the distance between the fitted sphere and the 3D points is above a threshold.

Note that the relative position of the triangulated points is correct, but their absolute depth can be recovered up to an unknown multiple of the stride since the planes are not distinguishable one from the other. In other words, matching between a certain 2D point and the bundle plane from which it was originated is somehow arbitrary. This is not a showstopper for many industrial applications, especially when the goal is to recover the shape of the surface and not its position, which is often the case with quality assurance. In cases where the absolute position of the surface is also needed, it would be straightforward to set an absolute numbering for stripes, for instance by using a special marker embedded in the pattern.

2.1 Implementation Details

The whole calibration procedure is sketched in Figure 3. We start by projecting the stripe pattern to the calibration sphere placed at different random positions in front of the camera. Stripe contour points are extracted by applying a series of image filters: first, 5 binary images are obtained by applying 5 different threshold levels to the original image. The skeletonization for each binary image is computed, as described in (Lee et al., 1994), to generate a set of 5 binarized skeleton masks. Then, the skeleton masks are summed into an accumulator in which morphological dilation is applied to join the isolated portions of each arc (ie. close small holes of the original skeleton masks). Finally, the accumulator is thresholded to extract all the connected components representing candidate ellipse arcs to be tested.

To provide a reliable an accurate ellipse fitting, we adopted a RANSAC-based approach as described in (Halır and Flusser, 1998). We filtered all the ellipses with less than 80% inliers among the point data, considering a RANSAC inlier distance of 2 camera pixels. In this way, all the extracted arcs that are not ellipses in the image are automatically discarded.

An additional inlier selection is then performed over the set of ellipses by fitting a line through their centres and checking their relative distance in pixels. Then, the ellipses whose centres are not uniformly distributed along the line are discarded (See. Alg.1). In Figure 3 (third image) the inlier ellipses used to

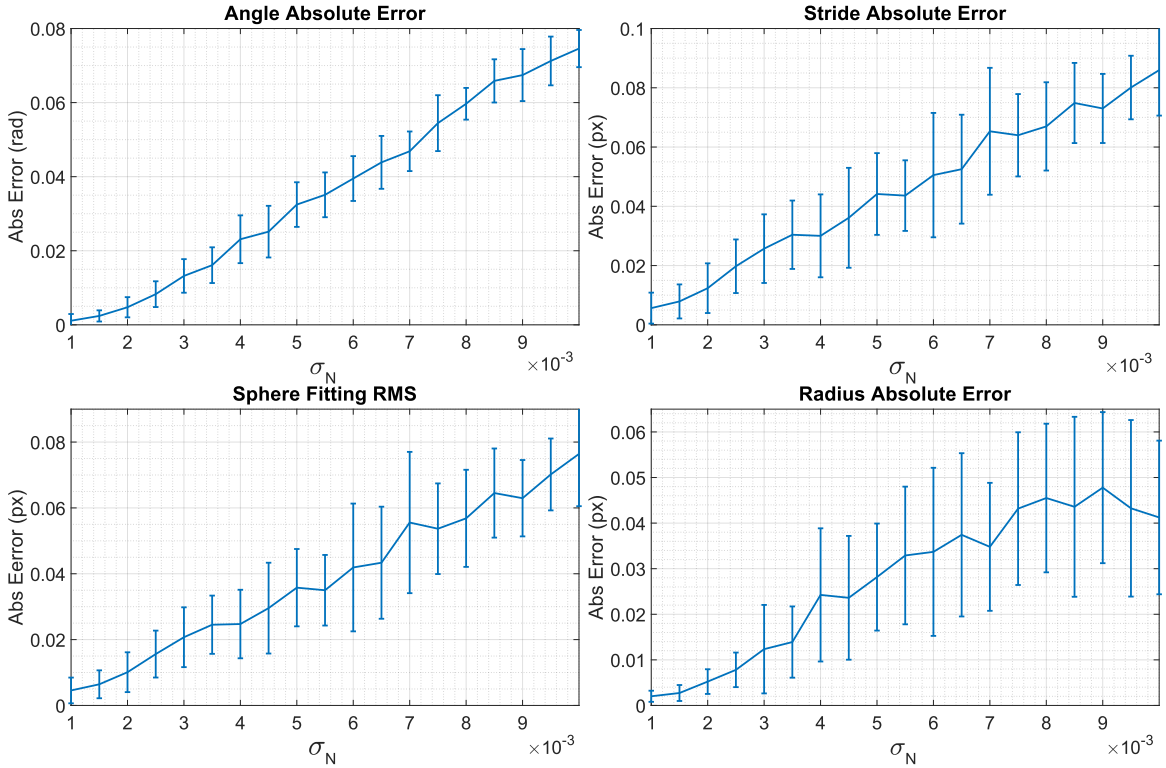

Figure 4: Calibration absolute errors on a synthetic scene. 2D ellipse points are perturbed with a zero-mean Gaussian random noise with standard deviation σ_N. For each noise level, the calibration is repeated several times measure the error against the ground truth.

Algorithm 1 Ellipse inlier detection

$c_1 \dots c_N \leftarrow$ centres of $E_1 \dots E_n$
fit a line l trough $c_1 \dots c_N$ via RANSAC
$\mathcal{S} \leftarrow$ set of indices i such that $\text{dist}(c_i, l) < t_l$
$\hat{c} = \frac{1}{|\mathcal{S}|} \sum_{i \in \mathcal{S}} c_i$
$\hat{l} \leftarrow$ fit a line through points in $\mathcal{S}$
$\mathcal{K} \leftarrow \langle\rangle$
for $i \in \mathcal{S}$ **do**
  $\hat{c}_i \leftarrow$ project c_i to $\hat{l}$
  add $\hat{c}_i$ in $\mathcal{K}$
end for
Sort points in K according to their signed distance to $\hat{c}$
$m \leftarrow |\mathcal{K}| - 1$
Compute $\langle \hat{d}_1 \dots \hat{d}_m \rangle$ where $\hat{d}_k = \| \mathcal{K}_{k+1} - \mathcal{K}_k \|$
$D \leftarrow \text{median}(\langle \hat{d}_1 \dots \hat{d}_m \rangle)$
Inliers $\leftarrow$ points in $\mathcal{K}$ s.t. $\text{dist}(\hat{d}_i, D) < t_d$

calibrate the system are displayed.

At this point, the selected ellipses are used to compute the plane normal and the stride value as described in the previous section. In practice, every ellipse gives a independent estimation of $\mathbf{n}$ and Δ. We simply average all such estimations to reduce the error. Then, the points belonging to the ellipses are triangulated and used to fit a 3D sphere with a standard linear least-squares approach. Finally, the pixel scale s is recovered as in (5). Figure 3 (right) shows an example of the resulting triangulated points and the corresponding fitted sphere.

3 EXPERIMENTAL EVALUATION

In order to evaluate the performances and the stability of the proposed method, we designed a set of synthetic and real-world experiments. First, we tested the accuracy of the parameter estimation from a single shot, introducing some noise and varying the system configuration. Then, we exploited our setup to validate the algorithm stability in the case of real-world applications.

3.1 Synthetic Validation

Synthetic tests give us the full control over the scene, allowing for a systematic validation of the proposed technique. We first decided to test the accuracy of the calibration method against acquisition noise, then

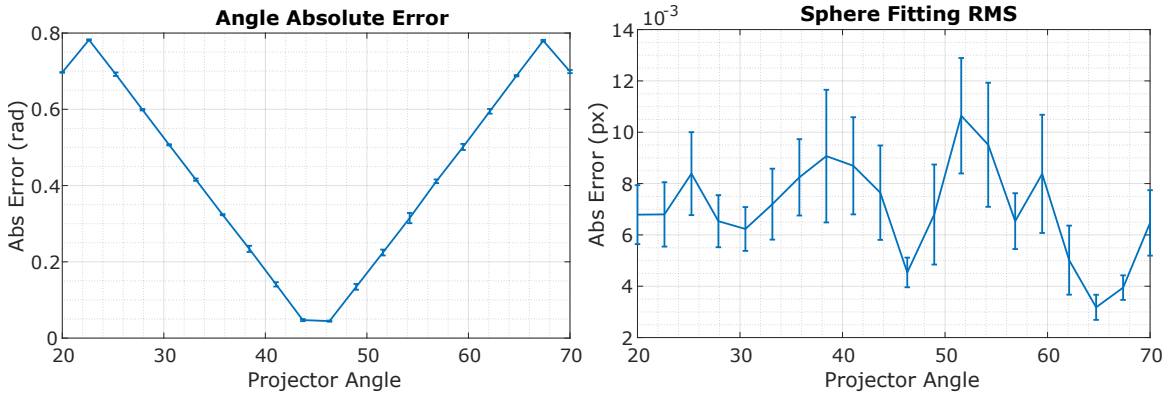

Figure 5: Results on a synthetic scene increasing angle between camera and projector.

we analysed the behaviour of the system varying the relative position between projector and camera. In our synthetic tests we simulated a configuration similar to the real setup, with a virtual orthographic camera and projector. The projector emits a set of 20 parallel planes with a fixed stride equal to 0.5 (camera px), and the camera captures a sphere with a radius equal to 3 pixels.

In the first experiment we fixed the projector orientation to 45 degrees with respect to the camera z-axis. Then, we randomized the sphere position (simulating a real acquisition) and perturbed the projected 2D points of each ellipse with a zero-mean Gaussian noise with standard deviation σ_N. Results are shown in Figure 4, where the absolute errors with respect to the ground truth are plotted. We increased the error standard deviation σ_N applied to 2D points and measured (i) the angle error with respect the plane normals, (ii) the stride error, (iii) the sphere radius estimation error, and (iv) the Root Mean Square (RMS) error of the triangulated points with respect to the sphere surface.

We repeated each test 100 times, with different sphere locations, using only one picture to calibrate the system. As expected, the errors increase linearly with the noise. In particular, for relatively small perturbations, the angle absolute error is smaller than 0.05 radians, and the sphere radius estimation error is below 0.03 pixels, that is the 2% of the actual radius.

As a second test, we analysed the impact of the relative angle between the projector and the camera. Indeed, since the observed portions of ellipses are fundamental to devise the final system parameters, we studied such effect on our synthetic setup to design an optimal configuration for our real-world prototype. To do so, we basically repeated the previous test, this time varying the relative angle between the camera and the projector z-axes. Note that with an angle close to 0 degrees the camera observes straight lines, because the plane normals are orthogonal to its z-axis, while when the angle is 90 degrees the camera should observe circle arcs. Results of this tests are shown in Figure 5. Interestingly, the projector angle exhibits a very high impact on the plane normal estimation, with an optimal orientation equal to 45 degrees. Other measurements are slightly affected by such angle, as shown for the sphere RMS.

3.2 Real-world Results

In our real-world tests we employed a camera-projector pair, both equipped with telecentric lenses. The camera acquires greyscale images with a 12 MPixels resolution, and we used a line pattern with a physical stride of 0.05 mm. The devices were mounted on a solid structure with a relative angle of approximately 45°, in a way that the plane of focus for both camera and projector are aligned to a common area of interest (see Fig. 1 and 7). The sphere used for calibration is a smooth ceramic bearing ball with a diameter of 8 mm and a declared surface tolerance of 0.7 microns.

We evaluated the accuracy and repeatability of the calibration varying the number of sphere acquisitions. A total of 30 images were acquired, varying the position of the sphere in the camera-projector frustum. Then, we used a cross-validation approach working as follows. The set of 30 images is divided in m partitions. For m times, one partition is used for calibration and the remaining $m-1$ for testing. The operation is repeated varying the number of partitions (and consequently the number of image samples used for calibration, in x-axis) and plotted in Fig.6. Each test was repeated 20 times, and the standard errors are also shown as error bars.

We can observe that the normal estimation er-

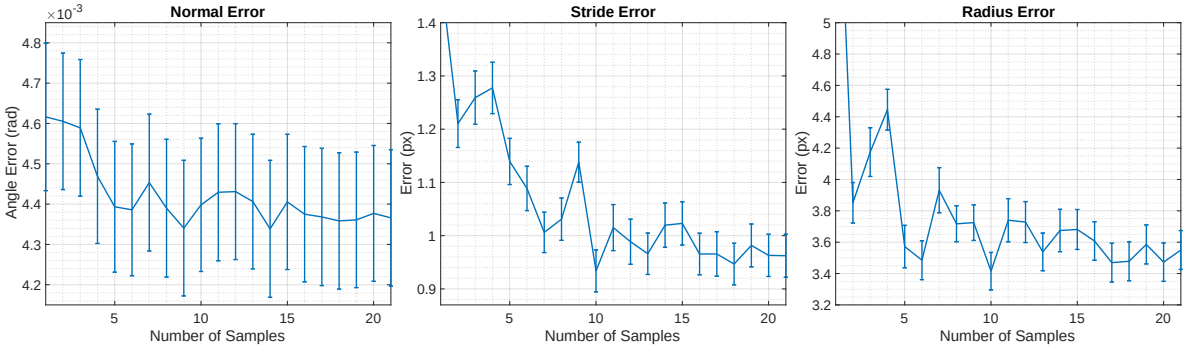

Figure 6: Calibration parameters estimation errors varying the number of acquisitions. From left to right: planes normal absolute error (rad), stride absolute error (px), and radius error (px).

ror between calibration and test set is in the order of $4.4 \cdot 10^{-3}$ radians, the stride error lower than 1.5 camera pixels and sphere radius absolute error consistently lower than 4 camera pixels for a number of calibration samples greater than 5. Moreover, the RMS of triangulated points over the fitted sphere is below 1 px for the majority of the acquired images. Considering that the computed scale (ie. the camera pixel size) s is $3.24 \cdot 10^{-3}$ mm/px, such error is approximately 6.5 microns.

We also tested the 3D reconstruction accuracy by means of the RMS error between the reconstructed 3D points and the ideal sphere calibration target. Overall, it ranges from 0.3 to 1.7 pixels, corresponding to 5 microns on average.

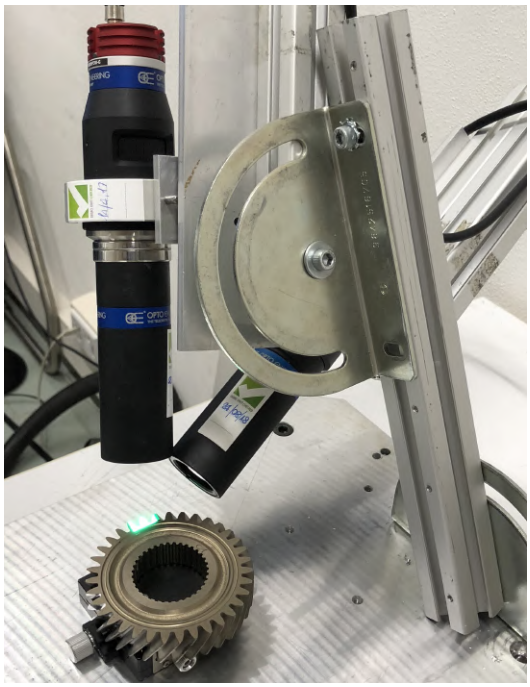

Figure 7: Our prototype setup to analyse the internal gearwheel's surfaces

4 APPLICATION: INDUSTRIAL SURFACE ANALYSIS

In this section we present an industrial application of our setup to acquire and analyse the internal gearwheel surfaces during the final steps of their production (Fig.7).

Gearwheels manufacturing is a field in which precision and repeatability is critical since the gear's teeth need to perfectly fit the shape of other similar components in a mechanical machinery.

When illuminated by our stripe projector and acquired by the camera, the teeth surface appears as a semi-shiny material, characterised by diffused microscratches as shown in Fig. 8a.

For this application we first apply a sequence of image filters so that the line pattern profiles are accurately extracted.

The result of image pre-processing task is shown in Figure 8b, where each extracted curve is highlighted in yellow. For each detected curve, a spline is fitted and then adjacent curves are identified in order to enumerate each subsequent projector plane. The actual teeth reconstruction is carried out by triangulating the detected splines. This is done first by uniformly sampling a set of discrete 2D point from each curve, and then by intersecting each point with the corresponding plane of $\mathcal{P}$. The procedure generates a 3D point cloud composed by the union of individual sampled curves, shown in Figure 8c.

Then, adjacent curves are analysed to find point-to-point correspondences between them. This is performed by running the Iterative Closest Point (Besl and McKay, 1992) algorithm between two adjacent curves to find their optimal alignment. The point matches given by the last iteration of ICP are used to synthetize additional points by uniform sampling 3D points on the straight lines connecting them.

Finally, Delaunay 2D triangulation (Chen and

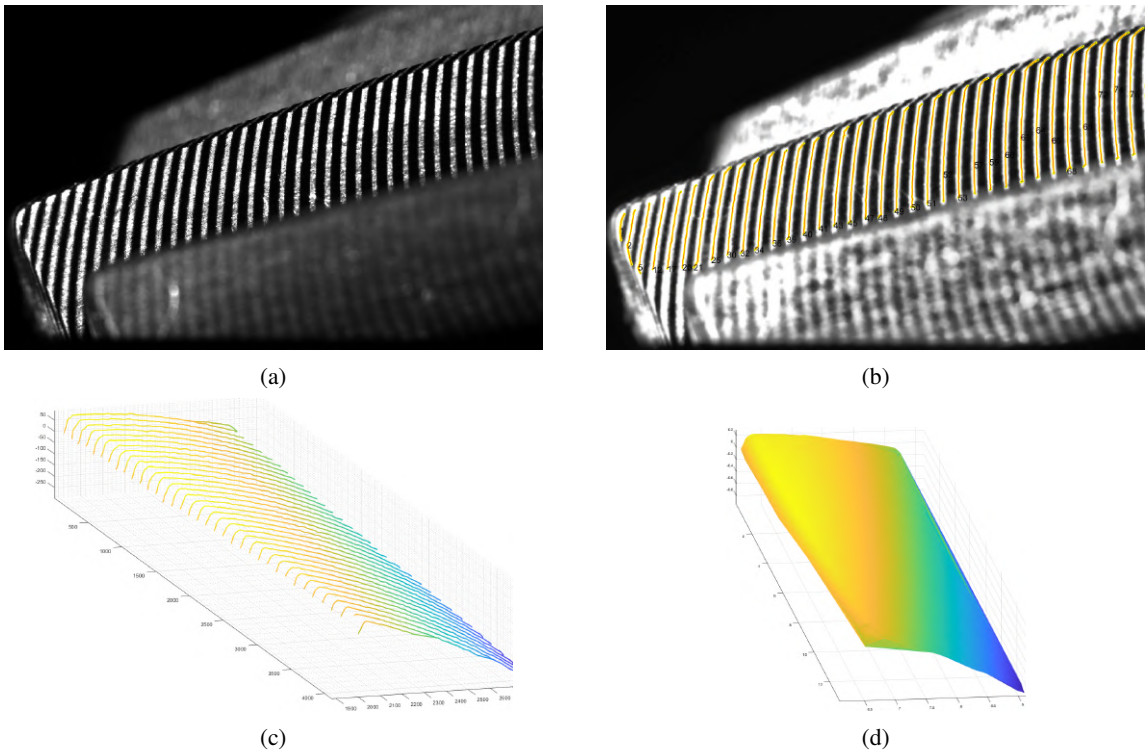

(a) (b) (c) (d)

Figure 8: Gearwheel teeth analysis. (a) image acquired by the camera. (b) Striped-pattern curve detection. (c) 3D point cloud obtained by triangulating each stripe. (d) Final tooth surface reconstruction (colour denotes z-coordinate to highlight the curvature).

Bishop, 1997) is applied to join the 2D points projections on the camera image plane and obtain a dense triangulated surface. An example of the final result is shown in Fig. 8d.

5 CONCLUSIONS

In this paper we proposed a micrometric calibration process for telecentric camera-projector setups, employing a fixed-striped pattern. We used a known spherical target to retrieve the geometrical characteristics of the system with a precision that can reach the order of microns. Since such targets are easy to manufacture and not expensive compared to their dimensional accuracy, the whole procedure can be carried out with a limited effort and costs. Synthetic and real-world experiments confirm both the stability of our method and its level of accuracy.

Additionally, we described a case-study of such a system, by means of a complete pipeline for microscopic surface acquisition and reconstruction involving micrometric gearwheel surface measurements.

REFERENCES

Bergamasco, F., Albarelli, A., and Torsello, A. (2011). Image-space marker detection and recognition using projective invariants. pages 381–388. cited By 14.

Bergamasco, F., Cosmo, L., Albarelli, A., and Torsello, A. (2014). Camera calibration from coplanar circles. pages 2137–2142.

Bergamasco, F., Pistellato, M., Albarelli, A., and Torsello, A. (2020). Cylinders extraction in non-oriented point clouds as a clustering problem. *Pattern Recognition*, 107. cited By 1.

Bergström, P., Rosendahl, S., and Sjödahl, M. (2011). Shape verification aimed for manufacturing process control. *Optics and Lasers in Engineering*, 49(3):403–409.

Besl, P. J. and McKay, N. D. (1992). Method for registration of 3-d shapes. In *Sensor fusion IV: control paradigms and data structures*, volume 1611, pages 586–606. International Society for Optics and Photonics.

Chen, H. and Bishop, J. (1997). Delaunay triangulation for curved surfaces. *Meshing Roundtable*, pages 115–127.

Chen, K., Shi, T., Liu, Q., Tang, Z., and Liao, G. (2018). Microscopic three-dimensional measurement based on telecentric stereo and speckle projection methods. *Sensors*, 18(11):3882.

Chen, Z., Liao, H., and Zhang, X. (2014). Telecentric stereo

micro-vision system: Calibration method and experiments. *Optics and Lasers in Engineering*, 57:82–92.

Halır, R. and Flusser, J. (1998). Numerically stable direct least squares fitting of ellipses. In *Proc. 6th International Conference in Central Europe on Computer Graphics and Visualization. WSCG*, volume 98, pages 125–132. Citeseer.

Hartley, R. and Zisserman, A. (2003). *Multiple view geometry in computer vision*. Cambridge university press.

Lee, T.-C., Kashyap, R. L., and Chu, C.-N. (1994). Building skeleton models via 3-d medial surface axis thinning algorithms. *CVGIP: Graphical Models and Image Processing*, 56(6):462–478.

Lei, S. and Zhang, S. (2009). Flexible 3-d shape measurement using projector defocusing. *Optics letters*, 34(20):3080–3082.

Li, B. and Zhang, S. (2015). Flexible calibration method for microscopic structured light system using telecentric lens. *Optics express*, 23(20):25795–25803.

Li, B. and Zhang, S. (2017). Microscopic structured light 3d profilometry: Binary defocusing technique vs. sinusoidal fringe projection. *Optics and Lasers in Engineering*, 96:117–123.

Li, D., Liu, C., and Tian, J. (2014). Telecentric 3d profilometry based on phase-shifting fringe projection. *Optics express*, 22(26):31826–31835.

Liu, C., Chen, L., He, X., Thang, V. D., and Kofidis, T. (2015). Coaxial projection profilometry based on speckle and fringe projection. *Optics Communications*, 341:228–236.

Liu, H., Lin, H., and Yao, L. (2017). Calibration method for projector-camera-based telecentric fringe projection profilometry system. *Optics express*, 25(25):31492–31508.

Pistellato, M., Bergamasco, F., Albarelli, A., Cosmo, L., Gasparetto, A., and Torsello, A. (2019a). Robust phase unwrapping by probabilistic consensus. *Optics and Lasers in Engineering*, 121:428–440. cited By 4.

Pistellato, M., Bergamasco, F., Albarelli, A., Cosmo, L., Gasparetto, A., and Torsello, A. (2019b). Stochastic phase estimation and unwrapping. pages 200–209. cited By 0.

Pistellato, M., Bergamasco, F., Albarelli, A., and Torsello, A. (2015). Dynamic optimal path selection for 3d triangulation with multiple cameras. *Lecture Notes in Computer Science (including subseries Lecture Notes in Artificial Intelligence and Lecture Notes in Bioinformatics)*, 9279:468–479.

Pistellato, M., Bergamasco, F., Albarelli, A., and Torsello, A. (2019c). Robust cylinder estimation in point clouds from pairwise axes similarities. pages 640–647.

Pistellato, M., Cosmo, L., Bergamasco, F., Gasparetto, A., and Albarelli, A. (2018). Adaptive albedo compensation for accurate phase-shift coding. volume 2018-August, pages 2450–2455. cited By 3.

Rosendahl, S., Hällstig, E., Gren, P., and Sjödahl, M. (2010). Shape measurement with one fringe pattern recording including a digital master. *Applied Optics*, 49(14):2622–2629.

Saeed, G. and Zhang, Y. (2007). Weld pool surface depth measurement using a calibrated camera and structured light. *Measurement Science and Technology*, 18(8):2570.

Weckenmann, A., Peggs, G., and Hoffmann, J. (2006). Probing systems for dimensional micro-and nanometrology. *Measurement Science and Technology*, 17(3):504.

Winkelbach, S. and Wahl, F. M. (2002). Shape from single stripe pattern illumination. In *Joint Pattern Recognition Symposium*, pages 240–247. Springer.

Xu, J., Xi, N., Zhang, C., Shi, Q., and Gregory, J. (2011a). Real-time 3d shape inspection system of automotive parts based on structured light pattern. *Optics & Laser Technology*, 43(1):1–8.

Xu, J., Xi, N., Zhang, C., Zhao, J., Gao, B., and Shi, Q. (2011b). Rapid 3d surface profile measurement of industrial parts using two-level structured light patterns. *Optics and Lasers in Engineering*, 49(7):907–914.

Yao, M. and Xu, B. (2007). Evaluating wrinkles on laminated plastic sheets using 3d laser scanning. *Measurement Science and Technology*, 18(12):3724.

Zhou, P., Zhu, J., Su, X., Jing, H., and Zhang, X. (2017). Three-dimensional shape measurement using color random binary encoding pattern projection. *Optical Engineering*, 56(10):104102.

Zuo, C., Feng, S., Huang, L., Tao, T., Yin, W., and Chen, Q. (2018). Phase shifting algorithms for fringe projection profilometry: A review. *Optics and Lasers in Engineering*, 109:23–59.